Solar RRL
www.solar-rrl.com

Check for updates

# Solution-Processed Electron-Selective Contacts Enabling 21.8% Efficiency Crystalline Silicon Solar Cells

*Wenjie Wang, Jian He,* Lun Cai, Zilei Wang, Siva Krishna Karuturi, Pingqi Gao, and Wenzhong Shen**

**Crystalline silicon (c-Si) solar cells with carrier-selective passivating contacts have been prosperously developed over the past few years, showing fundamental advantages, e.g., simpler configurations and higher potential efficiencies, compared with conventional c-Si solar cells using highly doped emitters. Herein, solution-processed cesium halides (CsX, X represents F, Cl, Br, I) are investigated as electron-selective contacts for c-Si solar cells, enabling lowest contact resistivity down to about 1 mΩ $cm^2$ for slightly doped n-type c-Si/CsF/Al contact. After inserting a thin intrinsic amorphous silicon (a-Si:H(i)) passivating layer, the contact resistivity can still be kept in a low value, about 10 mΩ $cm^2$. With full area rear-side a-Si:H(i)/CsF/Al electron-selective passivating contacts, record power conversion efficiencies of about 21.8% are finally demonstrated for n-type c-Si solar cells, showing a simple approach to realize high-efficiency c-Si solar cells.**

## 1. Introduction

Great breakthroughs have already been made in the power conversion efficiency (PCE) of conventional crystalline silicon (c-Si) solar cells in recent years, and the record PCE is getting close to the theoretical efficiency limit.[1] However, either high-temperature diffused p–n homojunction solar cells or doped amorphous silicon-based heterojunction solar cells cannot avoid the Auger recombination and free carrier recombination loss in the heavily doped layer, which restricts the theoretical efficiency limit of the c-Si solar cells.[1–4] The amorphous silicon layers in the heterojunction solar cells also face serious parasitic optical absorption.[5] In addition, from the perspective of device manufacturing, the complex fabrication processes, toxic dopants, high-temperature energy consumption, as well as the expensive equipment limit the further development of the process technology of c-Si solar cells. Therefore, developing simpler device structure and eliminating the use of heavily doping layer have an important impact on the further improvement of device efficiency. One of the potential candidates to overcome these drawbacks is the dopant-free carrier-selective contacted c-Si heterojunction solar cells.[6,7]

Taking n-type c-Si for example, the typical dopant-free carrier-selective c-Si heterojunction solar cells should contain the following layers: the holes and electrons transporting layers with high and low work functions matching the valence band and conduction band of the n-type c-Si, c-Si absorption layer, passivating layers, and the conductive electrodes.[8,9] On the hole contact side, when the hole transporting layer (HTL) is contacted with n-type c-Si, the large mismatch of work function between HTL and c-Si will induce a large upward band bend (built-in potential) on the c-Si surface, forming a strong inversion layer and driving the hole to HTL and the electron to the c-Si. Transition metal oxides (e.g., molybdenum oxide, tungsten oxide, and vanadium oxide), organic polymer (e.g., poly(3,4-ethylene dioxythiophene): poly(styrenesulfonate), and poly(3-hexylthiphene)), low-dimensional carbon materials (e.g., carbon nanotube and graphene) have been used as HTL.[10–21]

On the electron contact side, the main function of the electron transporting layer (ETL) is to eliminate the Schottky barrier caused by directly metal–semiconductor contact. Two approaches are generally used, and have already been successfully demonstrated in c-Si solar cells. One is to insert a thin ETL with very low work function (lower than metal electrode, e.g., Al) between the c-Si and metal electrode. This low work functional ETL will be able to make a downward band bend at c-Si side, and thus allow the transport of electrons from c-Si side to metal electrode side. Metal fluorides (e.g., lithium fluoride and magnesium fluoride), metal carbonates (e.g., cesium carbonate, potassium carbonate, and calcium carbonate), low work function metals (e.g., calcium and magnesium), and organic polymers (e.g., quinhydrone, poly(ethylene oxide), $C_{60}$ pyrrolidine tris-acid, and phenyl-$C_{61}$-butyric acid methyl ester) have been proven to be effective ETLs.[22–29] The other approach to realize effective electron-selective contact is to passivate the surface state density

W. Wang, Dr. W. Shen
Key Laboratory of Artificial Structures and Quantum Control (Ministry of Education) Institute of Solar Energy School of Physics and Astronomy
Shanghai Jiao Tong University
Shanghai 200240, China
E-mail: wzshen@sjtu.edu.cn

W. Wang, Dr. J. He, Dr. S. K. Karuturi
Research School of Electrical, Energy and Materials Engineering
The Australian National University
Canberra, ACT 2601, Australia
E-mail: jian.he@anu.edu.au

Dr. L. Cai, Z. Wang, Dr. P. Gao
School of Materials
Sun Yat-sen University
Guangzhou 510275, China

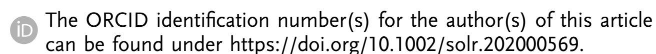
The ORCID identification number(s) for the author(s) of this article can be found under https://doi.org/10.1002/solr.202000569.

DOI: 10.1002/solr.202000569

 © 2020 Wiley-VCH GmbH

at c-Si/metal interface. For example, some metal oxides (e.g., titanium oxide, magnesium oxide, and tantalum oxide) and metal nitrides (e.g., titanium nitride, titanium oxynitride, and tantalum nitride) can form effective electron-selective contacts with n-type c-Si even if they do not have low work function.[30–38] This is mainly attributed to the thin silicon oxide ($SiO_x$) layers formed during the deposition processes, which can produce effective passivation on c-Si surface. Although high PCEs about 20% have been reported using these ETLs in c-Si solar cells, there is still room for further improvement. For example, low contact resistivity $\rho_c$ can be easily achieved using low work functional ETLs, however, these ETLs always have poor passivation to the c-Si surface, which limits the further improvement on the open-circuit voltage ($V_{OC}$) of the c-Si solar cells. As to the metal oxides or metal nitrides that can support good passivation to c-Si surface, the low conductivity, as well as their poor work functions make it difficult to achieve low contact resistivity, and thus limit the fill factor (FF) of the c-Si solar cells. Cesium salts, e.g., $CsCO_3$, and metal fluorides, e.g., $LiF_x$, have been proven to be effective electron-selective materials, even with well-passivated c-Si architecture (e.g., a-Si:H(i)/c-Si).[23,39] In this article, solution-processed cesium halides (CsX, X represents fluorine (F), chlorine (Cl), bromine (Br), and iodine (I)) are investigated as effective electron-selective contacts on well-passivated intrinsic amorphous silicon/c-Si (a-Si:H(i)/c-Si) architecture. A low contact resistivity $\rho_c$ of about 10 m$\Omega$ cm$^2$ is realized for n-type c-Si/a-Si:H(i)/CsF/Al contact, combined with a satisfied surface passivation (effective surface recombination velocity $S_{eff}$ about 5.7 cm s$^{-1}$). Using this electron-selective passivating contact, a satisfied PCE of 21.8% is finally realized for n-type c-Si solar cell, demonstrating an effective approach to fabricate high-efficiency c-Si solar cells with simplified fabrication processes.

## 2. Results and Discussion

The contact property of the CsX film on slightly doped n-type c-Si substrate was evaluated by measuring the contact resistivity $\rho_c$ of n-type c-Si/CsX/Al contact. **Figure 1**a shows the current–voltage (*I–V*) curves of n-type c-Si/Al contacts with and without CsX interlayers. For direct c-Si/Al contact, a typical rectification curve was shown in Figure 1a (black dotted line), which is resulted by the Fermi-level pinning of c-Si/Al contact. While spin-coating a thin CsX layer between c-Si and Al, the contact property is well improved, leading to a linear Ohmic contact. Figure 1b shows the CsX thickness (defined by the concentration of CsX from 0.5 to 20 mg mL$^{-1}$) dependent contact resistivity $\rho_c$ for c-Si/CsX/Al contacts. With the increase in the CsX concentration, a reduced contact resistivity $\rho_c$ can be observed for all of the CsX layers, which is likely attributed to the reduced work function and effective electron tunneling of CsX films. Further increasing the concentration of CsX films will lead to a higher contact resistivity $\rho_c$, possibly due to the bulk resistivity of CsX films. For all of the CsX films explored in this work, the incorporation of the CsX layers can effectively reduce the contact resistivity $\rho_c$ to the magnitude

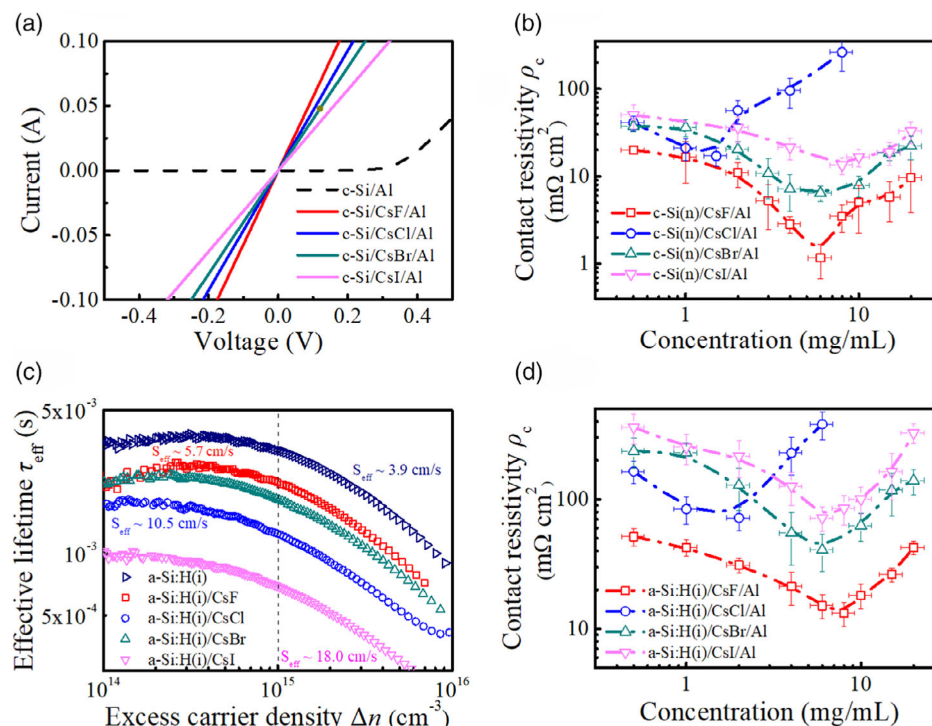


**Figure 1.** a) Current–voltage curves of n-type c-Si/Al contact with and without CsX interlayer. b) Contact resistivity $\rho_c$ of n-Si/CsX/Al contacts as a function of CsX concentration. c) Effective minority carrier lifetime of symmetrically passivated a-Si:H(i)/c-Si/a-Si:H(i) and CsX/a-Si:H(i)/c-Si/a-Si:H(i)/CsX. The effective surface recombination velocity $S_{eff}$ of these contacts were noted in panel (c) with the same color. d) Contact resistivity $\rho_c$ of n-Si/a-Si:H(i)/CsX/Al contacts as a function of CsX concentration.

 © 2020 Wiley-VCH GmbH

of about 10 mΩ cm$^2$. Especially, a minimized contact resistivity $\rho_c$ down to about 1 mΩ cm$^2$ is realized for c-Si/CsF/Al contact.

A satisfied carrier-selective passivating contact requires not only low contact resistivity but also high-quality surface passivation. To achieve high-performance surface passivation, a-Si:H(i) passivating layer with optimized thickness of about 6 nm is deposited on the c-Si surface.[6,10,38] Figure 1c shows the effective minority carrier lifetime of symmetrically structured a-Si:H(i)/c-Si/a-Si:H(i) and CsX/a-Si:H(i)/c-Si/a-Si:H(i)/CsX contacts. After depositing thin a-Si:H(i) passivating layers (≈6 nm) on the both sides, well-passivated interface with a low effective surface recombination velocity ($S_{eff}$) of about 3.9 cm s$^{-1}$ is achieved. However, after spin-coating CsX films on c-Si/a-Si:H(i) surface, the c-Si surface passivation is slightly degraded, showing the $S_{eff}$ values reduced from 3.9 to 5.7, 6.4, 10.5, and 18.0 cm s$^{-1}$ after spin-coating CsF, CsCl, CsBr, and CsI films, respectively. The best passivation quality is achieved by c-Si/a-Si:H(i)/CsF stack structure. The CsX thickness related to contact resistivity $\rho_c$ on c-Si/a-Si:H(i) surface is also shown in Figure 1d. Similar trend can be found compared with c-Si/CsX/Al contact. Eventually, an optimized contact resistivity of about 10 mΩ cm$^2$ can be extracted for the c-Si/a-Si:H(i)/CsF/Al contact, showing that this kind of spin-coated CsF film will be effective electron-selective material for the application of c-Si solar cells.

The ultraviolet photoelectron spectroscopy (UPS) spectrum was used to analyze the optoelectronic properties of the CsX films. **Figure 2**a shows the UPS secondary electron cutoff of the CsX films, showing low work function values of 2.96, 3.10, 3.30, and 3.52 eV for the CsF/Al, CsCl/Al, CsBr/Al, and CsI/Al interface, respectively. Compared with the work function of directly Al contact (about 4.2 eV), these low work function values of CsX films play a crucial role in forming Ohmic contact between n-type c-Si substrate and Al electrode. Figure 2b shows the UPS valence band spectrum of the CsX films. For the CsF films, the valence band is measured to be about 5.10 eV from the Fermi energy. However, for CsCl, CsBr, and CsI films, narrower gaps were measured, showing worse hole-blocking performance of these films. The X-ray photoelectron spectroscopy (XPS) core-level spectrum of Cs 3d is shown in Figure S1, Supporting Information, for all of the CsX films. Doublet peaks located close to ≈724 eV (3d 5/2) and ≈739 eV (3d 3/2) can be found for all the four halides.[40] However, gentle peak shift can be observed for these CsX films. The Cs element in CsCl film is measured to have the highest binding energy of about 727.1 eV, whereas the CsF film shows the lowest binding energy of about 725.1 eV. The slight shift of the binding energy is likely attributed to the difference of halogen anions.[40]

Figure 2c presents the energy band alignments of c-Si/Al contact with and without CsF electron-selective layer. As for the c-Si/Al contact, a Schottky barrier could be found at the interface according to Mott–Schottky theory and Fermi pinning effect, which blocks the electrons transport from c-Si to metal electrode.[33] After inserting a low work function CsF film between the c-Si and Al, a downward energy-band bending appears at the c-Si interface which enables electrons to easily transport from c-Si to Al. However, there are still large numbers of density of states at the contact interface due to the lack of passivation of CsF film, which results in serious carrier recombination at the interface. After further inserting a thin a-Si:H(i) passivating layer between the c-Si and CsF film, the carrier recombination at the interface can be well suppressed.

Thermal evaporation deposited CsF film has been proven to be effective electron-selective contact material in c-Si solar cells.[6] Compared with the CsF film deposited by thermal evaporation, the solution-processed CsF film shows better contact property to c-Si, as well as better long-term stability, as shown in **Figure 3**a. Even after about 1000 h storage, the contact resistivity $\rho_c$ still keeps a low value of about 5 mΩ cm$^2$ for the spin-coated samples

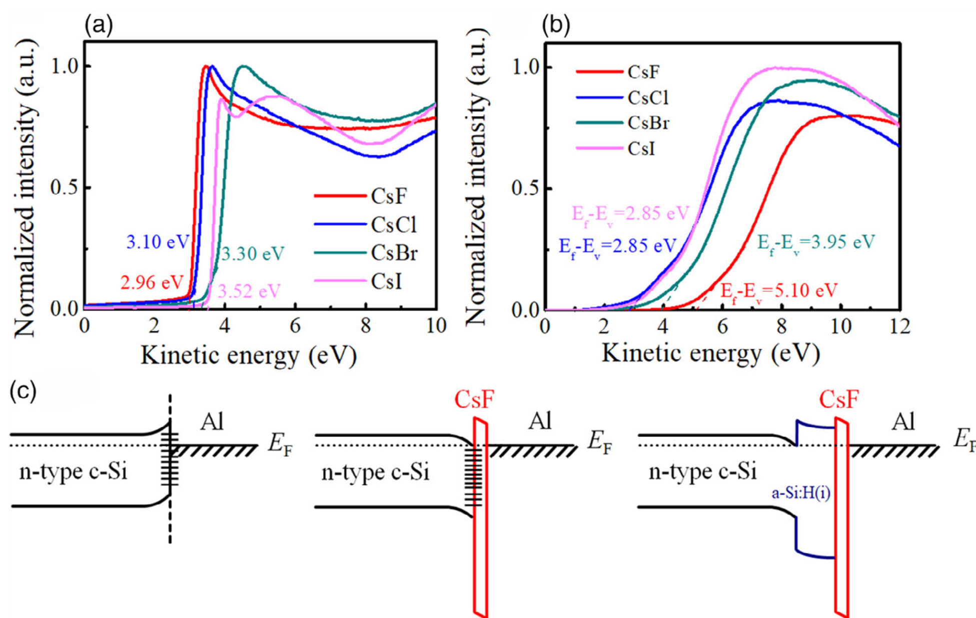


**Figure 2.** a) Work function value of CsX films extracted by UPS secondary electron cutoff spectrum. b) Valence band spectrum of the CsX films. c) Energy band diagrams of the direct n-type c-Si/Al contact, n-type c-Si/CsX/Al contact, and n-type c-Si/a-Si:H(i)/CsF/Al contact.


© 2020 Wiley-VCH GmbH

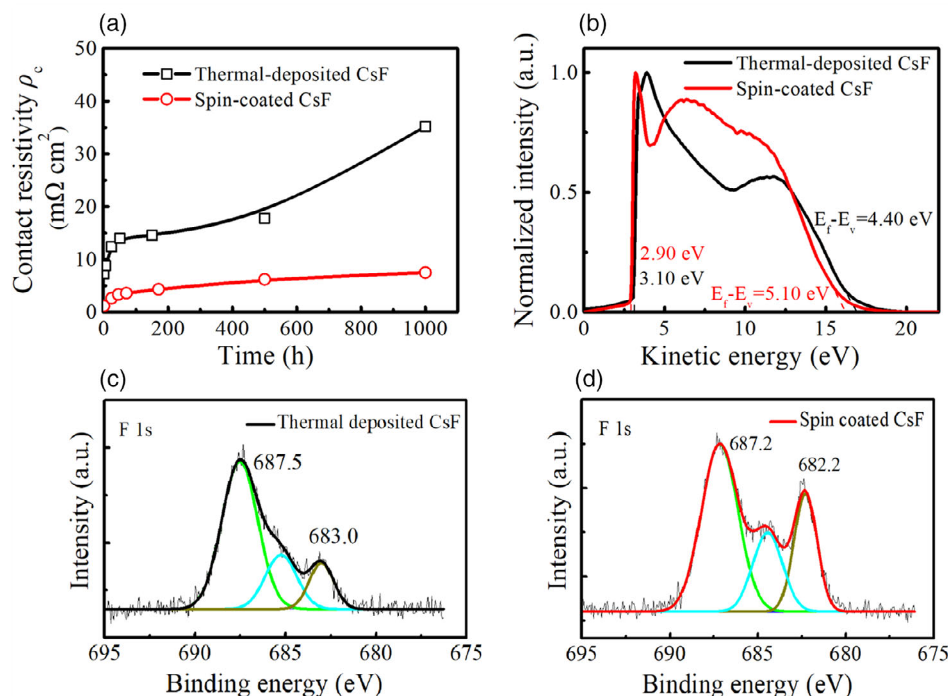


**Figure 3.** a) Contact resistivity stability of thermal-deposited CsF and spin-coated CsF film with test structure of c-Si/CsF/Al contact. b) The UPS spectra of thermal-deposited CsF film and spin-coated CsF film. The XPS of the F 1s core-level spectra of c) the thermal-deposited CsF film and d) the spin-coated CsF film.

while the contact resistivity $\rho_c$ degraded to about 35 mΩ cm$^2$ for the thermal-deposited CsF film. Figure 3b shows the UPS spectra of the spin-coated CsF film and thermal-deposited CsF film, displaying the work function values of 2.90 and 3.10 eV for the spin-coated CsF film and thermal-deposited CsF film, respectively. The valence band is measured to be about 5.10 eV from the Fermi energy for the spin-coated CsF film while that is about 4.40 eV for the thermal-deposited one, showing that the spin-coated CsF film has much better performance in electron collection as well as hole-blocking property. To explore the difference in these two films, the XPS spectra are shown in Figure 3c and Figure S2, Supporting Information. For Cs 3d spectra, the results seem almost the same as shown in Figure S2a,b, Supporting Information. However, for F 1s core-level spectra, a weaker peak can be found for the thermal-deposited CsF film at the binding energy of about 683 eV.[40] Based on core level peak areas shown in Figure 3c,d, the stoichiometry of the CsF films can be extracted. For spin-coated CsF film, stoichiometric film with F to Cs atomic fraction close to 1 can be found. However, the thermal-deposited CsF film shows nonstoichiometric with F to Cs atomic fraction less than 1.

To demonstrate the electron-selective properties of the spin-coated CsF film on the device level, full-area rear-side contacted proof-of-concept n-type c-Si solar cells were fabricated. **Figure 4**a shows the schematic structure of the n-type c-Si solar cell with a full-area rear a-Si:H(i)/CsF/Al electron-selective contact. On the front side, conventional diffused p$^+$n junction is used for the separation of photogenerated carriers. On the rear side, an a-Si:H(i) passivation layer combined with CsF ETL are used for the collection of electrons. Cross-sectional high-resolution transmission electron microscopy (HR-TEM) was used to characterize the c-Si/a-Si:H(i)/CsF/Al interface, as shown in Figure 4b, showing a clear hierarchical interface.

Figure 4c shows the characteristic $I$–$V$ curves of the c-Si solar cells using directly c-Si/Al contact, c-Si/CsF/Al contact, and c-Si/a-Si:H(i)/CsF/Al contact under one-sun standard illumination. Corresponding electrical output parameters are summarized in **Table 1**. For direct c-Si/Al contact, due to the poor rear contact, the c-Si solar cell shows an unsatisfied photovoltaic performance with PCE of about 16.2%, $V_{OC}$ of 0.588 V, short-circuit current density ($J_{SC}$) of 38.3 mA cm$^{-2}$, and FF of 0.717. After spin-coating a thin CsF interlayer between c-Si and Al, the c-Si/Al contact interface is well improved, regarding to a well-improved photovoltaic performance with the PCE increased to 19.4%, $V_{OC}$ to 0.621 V, $J_{SC}$ to 38.9 mA cm$^{-2}$, and FF of 0.803. The internal quantum efficiency (IQE) measurements are also utilized to characterize the rear-side contact property, as shown in Figure 4d. Compared with direct c-Si/Al contact, a significantly improvement in the quantum efficiency can be found in the near infrared range (800–1200 nm) for the c-Si solar cell using CsF/Al electron-selective contact, indicating that the electron collection efficiency is well improved at rear side. To further improve the interface passivation, a thin a-Si:H(i) passivating layer was deposited between c-Si and CsF by plasma-enhanced chemical vapor deposition (PECVD), demonstrating a record PCE of 21.8%, with a $V_{OC}$ of 0.688 V, $J_{SC}$ of 40.1 mA cm$^{-2}$, and FF of 0.789. The IQE results in Figure 4d also indicate that the quantum efficiency can be further improved in the infrared range by applying a-Si:H(i)/CsF/Al electron-selective contact, reflecting that the carrier recombination at rear side is significantly suppressed.


© 2020 Wiley-VCH GmbH

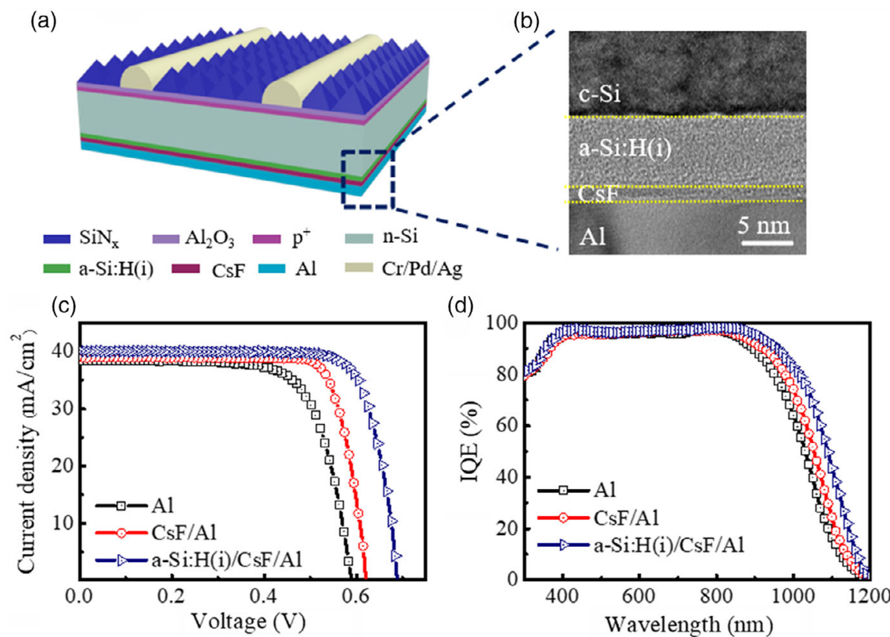


**Figure 4.** a) Schematic of n-type c-Si solar cell with a full-area rear a-Si:H(i)/CsF/Al electron-selective contact. b) Cross-sectional HR-TEM of the n-Si/a-Si:H(i)/CsF/Al contact. c) Light *I–V* curves of c-Si solar cells with direct c-Si/Al contact, c-Si/CsF/Al contact, and c-Si/a-Si:H(i)/CsF/Al contact under AM 1.5G and d) corresponding IQE curves.

**Table 1.** The photovoltaic performance parameters of the c-Si solar cells with different rear contacts under AM1.5G one-sun illumination.

| Samples | $V_{oc}$ [V] | $J_{sc}$ [mA/cm$^2$] | FF | PCE [%] |
|---|---|---|---|---|
| c-Si/Al | 0.588 | 38.3 | 0.717 | 16.2 |
| c-Si/CsF/Al | 0.621 | 38.9 | 0.803 | 19.4 |
| c-Si/a-Si:H(i)/CsF/Al | 0.688 | 40.1 | 0.789 | 21.8 |

## 3. Conclusion

In summary, we have investigated solution-processed CsX (X represents F, Cl, Br, I) films together with high-quality a-Si:H(i) passivating layer as an effective electron-selective passivating contacts. Among these candidates, CsF is found to be the best choice for c-Si solar cells. Optimized n-type c-Si/a-Si:H(i)/CsF/Al electron-selective passivating contact provides a low contact resistivity $\rho_c$ of about 10 m$\Omega$ cm$^2$ and an excellent surface passivation with $S_{eff}$ of about 5.7 cm s$^{-1}$. A satisfied PCE of 21.8% is finally realized for n-type c-Si solar cell with a full-area a-Si:H(i)/CsF/Al contact, demonstrating an effective approach to fabricate high-efficiency c-Si solar cells with simplified fabrication processes.

## 4. Experimental Section

*Contact and Passivation Measurement*: The contact resistivities were extracted by fitting the resistance with the electrode diameters using the method devised by Cox and Strack. Single-side polished n-type c-Si wafers with resistivity of 1–3 Ω cm were used. After removing the natural oxide layer by dilute hydrofluoric acid (HF, ≈2% concentration), c-Si wafers were spin-coated with CsX (X represents F, Cl, Br, I) solution with different concentration from 0.5 to 20 mg mL$^{-1}$ at spin speed of 3000 rpm. After that, Al electrodes with different diameters were thermally evaporated on the CsX films with thickness of 200 nm through a shadow mask. For a-Si:H(i) passivated samples, a-Si:H(i) layers with thickness of 6 nm were deposited by PECVD before CsX spin-coating. Double-side polished n-type c-Si wafers with resistivity of 1–5 Ω cm and thickness of 300 μm were used for passivation characterization. Following standard RCA cleaning and dilute HF dipping, a-Si:H(i) layers with thickness of about 6 nm were deposited symmetrically on the both sides of the wafers by PEVCD. CsX films were then symmetrically spin-coated on both sides of the wafer.

*Solar Cell Fabrication*: Standard c-Si solar cells were fabricated to evaluate the electron-selective properties of the CsF film. N-type (100)-oriented c-Si wafers (Cz, 180 μm thickness, and 1.0 Ω cm resistivity) were used here. Before front-side emitter diffusion, the wafers were immersed in tetrmethylammonium hydroxide (TMAH), isopropyl alcohol (IPA), and deionized (DI) water mixed solution at 85 °C for 60 min to fabricate random pyramidic structure for light-trapping. After texturing, the wafers were cleaned with standard RCA process and boron diffusion in tube furnace to form the front-side p$^+$ emitter (≈120 Ω sq$^{-1}$). Atomic layer deposition $Al_2O_3$ passivation layer (20 nm) and PECVD $SiN_x$ (65 nm) antireflection layer were then deposited on the top of the emitter. Front-side metal grid electrode were patterned by photolithography and thermally evaporated with Cr (≈10 nm)/Pd (≈10 nm)/Ag (≈100 nm) stack and then thickened by Ag electroplating. For the rear undiffused side, a-Si:H(i) passivating layer (6 nm) was deposited by PECVD and followed by spin-coating of CsF film. Full-area Al rear contact with thickness of 300 nm was finally deposited by thermal evaporation.

*Characterization*: Keithley 2400 source-meter was used to measure the contact resistivity. The effective excess carrier lifetimes of samples were characterized by photoconductance decay (Sinton WCT 120). XPS measurements were performed with a Thermo Scientific Escalab 250Xi spectrometer using the Al Kα X-ray source ($h\nu$ = 1486.6 eV). HR-TEM was used to characterize the rear-side contact interface. The photovoltaic

 © 2020 Wiley-VCH GmbH

performance of the c-Si solar cells was characterized by solar simulator (Sinton Instruments) with an Xe arc lamp under standard test conditions (Air-mass 1.5 illumination, $1000\,W\,m^{-2}$, $25\,°C$) with a $4\,cm^2$ shadow mask. An encapsulated standard reference c-Si solar cells certified by Fraunhofer CalLab was used to calibrate the illumination intensity. The quantum efficiency of the solar cells was measured by Protoflex Corporation QE measurement system.

## Supporting Information

Supporting Information is available from the Wiley Online Library or from the author.

## Acknowledgements

W.S. acknowledges the support from Major State Basic Research Development Program of China (2018YFB1500501), National Natural Science Foundation of China (11834011, 11974242). J.H. and S.K.K. acknowledge the financial support from the Australian Renewable Energy Agency (ARENA). P.G. acknowledges the support from National Natural Science Foundation of China (61974169, 61674154), Guangdong Basic and Applied Basic Research Foundation (2019B151502053).

## Conflict of Interest

The authors declare no conflict of interest.

## Keywords

cesium fluoride, contact resistivity, c-Si solar cells, electron-selective contacts, passivating contacts

Received: September 13, 2020
Revised: October 4, 2020
Published online: October 21, 2020

[1] T. G. Allen, J. Bullock, X. Yang, A. Javey, S. De Wolf, *Nat. Energy* **2019**, *4*, 914.
[2] D. Yan, A. Cuevas, *J. Appl. Phys.* **2013**, *114*, 044508.
[3] D. Yan, A. Cuevas, *J. Appl. Phys.* **2014**, *116*, 194505.
[4] M. Hermle, F. Feldmann, M. Bivour, J. C. Goldschmidt, S. W. Glunz, *Appl. Phys. Rev.* **2020**, *7*, 021305.
[5] Z. C. Holman, A. Descoeudres, L. Barraud, F. Z. Fernandez, J. P. Seif, S. De Wolf, C. Ballif, *IEEE J. Photovoltaics* **2012**, *2*, 7.
[6] J. Bullock, M. Hettick, J. Geissbühler, A. J. Ong, T. Allen, C. M. Sutter-Fella, T. Chen, H. Ota, E. W. Schaler, S. De Wolf, C. Ballif, A. Cuevas, A. Javey, *Nat. Energy* **2016**, *1*, 15031.
[7] J. Bullock, Y. Wan, Z. Xu, S. Essig, M. Hettick, H. Wang, W. Ji, M. Boccard, A. Cuevas, C. Ballif, A. Javey, *ACS Energy Lett.* **2018**, *3*, 508.
[8] C. Messmer, M. Bivour, J. Schön, M. Hermle, *J. Appl. Phys.* **2018**, *124*, 085702.
[9] C. Messmer, M. Bivour, J. Schon, S. W. Glunz, M. Hermle, *IEEE J. Photovoltaics* **2018**, *8*, 456.
[10] C. Battaglia, S. M. de Nicolás, S. De Wolf, X. Yin, M. Zheng, C. Ballif, A. Javey, *Appl. Phys. Lett.* **2014**, *104*, 113902.
[11] J. Bullock, A. Cuevas, T. Allen, C. Battaglia, *Appl. Phys. Lett.* **2014**, *105*, 232109.
[12] M. Bivour, J. Temmler, H. Steinkemper, M. Hermle, *Sol. Energy Mater. Sol. Cells* **2015**, *142*, 34.
[13] L. G. Gerling, S. Mahato, A. Morales-Vilches, G. Masmitja, P. Ortega, C. Voz, R. Alcubilla, J. Puigdollers, *Sol. Energy Mater. Sol. Cells* **2016**, *145*, 109.
[14] J. Dréon, Q. Jeangros, J. Cattin, J. Haschke, L. Antognini, C. Ballif, M. Boccard, *Nano Energy* **2020**, *70*, 104495.
[15] O. Almora, L. G. Gerling, C. Voz, R. Alcubilla, J. Puigdollers, G. Garcia-Belmonte, *Sol. Energy Mater. Sol. Cells* **2017**, *168*, 221.
[16] G. Masmitjà, L. G. Gerling, P. Ortega, J. Puigdollers, I. Martín, C. Voz, R. Alcubilla, *J. Mater. Chem. A* **2017**, *5*, 9182.
[17] X. Yang, H. Xu, W. Liu, Q. Bi, L. Xu, J. Kang, M. N. Hedhili, B. Sun, X. Zhang, S. De Wolf, *Adv. Electron. Mater.* **2020**, *6*, 2000467.
[18] J. He, Y. Wan, P. Gao, J. Tang, J. Ye, *Adv. Funct. Mater.* **2018**, *28*, 1802192.
[19] F. S. Freitas, R. B. Merlo, F. C. Marques, A. F. Nogueira, *Phys. Status Solidi A* **2014**, *211*, 2657.
[20] D. D. Tune, B. S. Flavel, R. Krupke, J. G. Shapter, *Adv. Energy Mater.* **2012**, *2*, 1043.
[21] D. Xu, X. Yu, L. Yang, D. Yang, *J. Electron. Mater.* **2018**, *47*, 5025.
[22] J. Bullock, P. Zheng, Q. Jeangros, M. Tosun, M. Hettick, C. M. Sutter-Fella, Y. Wan, T. Allen, D. Yan, D. Macdonald, S. De Wolf, A. Hessler-Wyser, A. Cuevas, A. Javey, *Adv. Energy Mater.* **2016**, *6*, 1600241.
[23] Y. Zhang, R. Liu, S. T. Lee, B. Sun, *Appl. Phys. Lett.* **2014**, *104*, 083514.
[24] Y. Wan, C. Samundsett, J. Bullock, T. Allen, M. Hettick, D. Yan, P. Zheng, X. Zhang, J. Cui, J. McKeon, A. Javey, A. Cuevas, *ACS Appl. Mater. Interfaces* **2016**, *8*, 14671.
[25] Y. Wan, J. Bullock, M. Hettick, Z. Xu, C. Samundsett, D. Yan, J. Peng, J. Ye, A. Javey, A. Cuevas, *Adv. Energy Mater.* **2018**, *8*, 1800743.
[26] T. G. Allen, J. Bullock, P. Zheng, B. Vaughan, M. Barr, Y. Wan, C. Samundsett, D. Walter, A. Javey, A. Cuevas, *Prog. Photovol.* **2017**, *25*, 636.
[27] Z. Zou, W. Liu, D. Wang, Z. Liu, E. Jiang, S. Wu, J. Zhu, W. Guo, J. Sheng, J. Ye, *Sol. Energy Mater. Sol. Cells* **2018**, *185*, 218.
[28] M. H. Yun, J. W. Kim, S. Y. Park, D. S. Kim, B. Walker, J. Y. Kim, *J. Mater. Chem. A* **2016**, *4*, 16410.
[29] W. Ji, T. Allen, X. Yang, G. Zeng, S. De Wolf, A. Javey, *ACS Energy Lett.* **2020**, *5*, 897.
[30] X. Yang, Q. Bi, H. Ali, K. Davis, W. V. Schoenfeld, K. Weber, *Adv. Mater.* **2016**, *28*, 5891.
[31] X. Yang, K. Weber, Z. Hameiri, S. De Wolf, *Prog. Photovoltaics Res. Appl.* **2017**, *25*, 896.
[32] J. Bullock, Y. Wan, M. Hettick, X. Zhaoran, S. P. Phang, D. Yan, H. Wang, W. Ji, C. Samundsett, Z. Hameiri, D. Macdonald, A. Cuevas, A. Javey, *Adv. Energy Mater.* **2019**, *9*, 1803367.
[33] Y. Wan, C. Samundsett, J. Bullock, M. Hettick, T. Allen, D. Yan, J. Peng, Y. Wu, J. Cui, A. Javey, A. Cuevas, *Adv. Energy Mater.* **2017**, *7*, 1601863.
[34] J. Yu, M. Liao, D. Yan, Y. Wan, H. Lin, Z. Wang, P. Gao, Y. Zeng, B. Yan, J. Ye, *Nano Energy* **2019**, *62*, 181.
[35] Y. Wan, S. K. Karuturi, C. Samundsett, J. Bullock, M. Hettick, D. Yan, J. Peng, P. R. Narangari, S. Mokkapati, H. H. Tan, C. Jagadish, A. Javey, A. Cuevas, *ACS Energy Lett.* **2017**, *3*, 125.
[36] X. Yang, E. Aydin, H. Xu, J. Kang, M. Hedhili, W. Liu, Y. Wan, J. Peng, C. Samundsett, A. Cuevas, S. De Wolf, *Adv. Energy Mater.* **2018**, *8*, 1800608.
[37] X. Yang, W. Liu, M. De Bastiani, T. Allen, J. Kang, H. Xu, E. Aydin, L. Xu, Q. Bi, H. Dang, E. AlHabshi, K. Kotsovos, A. AlSaggaf, I. Gereige, Y. Wan, J. Peng, C. Samundsett, A. Cuevas, S. De Wolf, *Joule* **2019**, *3*, 1314.
[38] X. Yang, Y. Lin, J. Liu, W. Liu, Q. Bi, X. Song, J. Kang, F. Xu, L. Xu, M. N. Hedhili, D. Baran, X. Zhang, T. D. Anthopoulos, S. De Wolf, *Adv. Mater.* **2020**, *32*, 2002608.
[39] Y. Zhang, W. Cui, Y. Zhu, F. Zu, L. Liao, S. T. Lee, B. Sun, *Energy Environ. Sci.* **2015**, *8*, 297.
[40] W. E. Morgan, J. R. V. Wazer, W. J. Stec, *J. Am. Chem. Soc.* **1973**, *95*, 751.


© 2020 Wiley-VCH GmbH